Magneto-optical transport properties of monolayer transition metal dichalcogenides

Nguyen D. Hien,[1,2,*] Chuong V. Nguyen,[3] Nguyen N. Hieu,[4] S. S. Kubakaddi,[5] C. A. Duque,[6] M. E. Mora-Ramos,[7] Le Dinh,[8] Tran N. Bich,[9] and Huynh V. Phuc[10,†]

[1]*Laboratory of Magnetism and Magnetic Materials, Advanced Institute of Materials Science, Ton Duc Thang University, Ho Chi Minh City 758307, Vietnam*

[2]*Faculty of Applied Sciences, Ton Duc Thang University, Ho Chi Minh City 758307, Vietnam*

[3]*Department of Materials Science and Engineering, Le Quy Don Technical University, Hanoi 100000, Vietnam*

[4]*Institute of Research and Development, Duy Tan University, Da Nang 550000, Vietnam*

[5]*Department of Physics, K. L. E. Technological University, Hubballi-580 031, Karnataka, India*

[6]*Grupo de Materia Condensada-UdeA, Instituto de Física, Facultad de Ciencias Exactas y Naturales, Universidad de Antioquia UdeA, Calle 70 No. 52-21, Medellín, Colombia*

[7]*Centro de Investigación en Ciencias-IICBA. Universidad Autónoma del Estado de Morelos. Av. Universidad 1001, CP 62209, Cuernavaca, Morelos, Mexico*

[8]*Center for Theoretical and Computational Physics, University of Education, Hue University, Hue 530000, Vietnam*

[9]*Physics Department, University of Education, Hue University, Hue 530000, Vietnam*

[10]*Division of Theoretical Physics, Dong Thap University, Cao Lanh 870000, Vietnam*

(Received 8 November 2019; revised manuscript received 1 January 2020; published 17 January 2020)

We study the optical transport properties of the monolayer transition metal dichalcogenides (TMDCs) such as MoS_2, WS_2, $MoSe_2$, and WSe_2 in the presence of a magnetic field. The TMDCs band structures are obtained and discussed by using the effective massive Dirac model, in which the spin and valley Zeeman effects as well as an external electric field are included. The magneto-optical absorption coefficient (MOAC) is derived as a function of absorbed photon energy when the carriers are scattered by random impurities combined with the intrinsic acoustic and optical phonons in TMDCs and the surface optical (SO) phonons of substrates. Our result shows that the spin-splitting feature appeared in all four TMDC materials. The combination of strong spin-orbit coupling (SOC) and Zeeman fields has doubled the Landau levels but has not changed the energy gap of the TMDCs monolayer, which can be controlled by the electric field. Because of their strong SOC effect, the absorption spectrum in monolayer TMDCs is separated into two separate peaks caused by spin up and down. At the low temperature, the MOAC intensity via impurity scattering is the biggest followed by that of the SO phonons while the intrinsic acoustic and optical phonon scatterings display the smallest. For the monolayer TMDCs on substrates, SiO_2 always shows its superiority in comparison with the others. Among the four TMDC materials, $MoSe_2$ shows the biggest MOAC intensity, while WS_2 has the biggest value of the absorbed photon energy. The full-width at half-maximum (FWHM) via impurity scattering achieves its highest value in WS_2, while this occurs in $MoSe_2$ and MoS_2 via intrinsic acoustic and optical phonon scatterings, respectively. Our estimation of mobility from FWHM gives good agreement with the experimental results in WS_2.

DOI: 10.1103/PhysRevB.101.045424

I. INTRODUCTION

The transition metal dichalcogenides (TMDCs), with chemical formula MX_2 (M = Mo, W, and X = S, Se), are the new two-dimensional (2D) material types, which are composed of 2D X-M-X layers, stacked together, and linked by a weak van der Waals interlayer coupling [1]. For the bulk configuration, the M atoms are arranged in a triangular structure, in which each M atom is bound to six atoms of chalcogenides X: three are in the top layer and three are in the bottom one, to create a sandwiched material. In contrast to graphene [2], a typical example of the gapless Dirac material, or boron nitride [3], a wide gap insulator, the TMDCs are the semiconducting materials of strong spin-orbit coupling (SOC) and large natural band gap. Another interesting feature of TMDCs is the dependence of their electronic band structures on the layer numbers: The transition from an indirect band gap in the case of multilayer samples to a direct band gap for monolayers. It makes this family of materials possessing remarkable electronic and optical properties [4], leading them to be hopeful candidates for next generation of optoelectronics devices [5] and to be one of the most crucial research topics in recent years.

Magneto-optical transport is one of the most important properties of the TMDCs which has been vastly investigated in both theoretical [6–10] and experimental [11–16] aspects. Most of these works are concentrated on the magneto-optical transitions in the monolayer of TMDCs using different techniques. A momentum balance equation approach is used to calculate the magnetoresistance in MoS_2 in the presence of interaction between the carriers with the impurity and many kinds of phonons [6]. However, in this work, the effect of

*nguyendinhhien@tdtu.edu.vn

†Corresponding author: hvphuc@dthu.edu.vn

Zeeman fields has not been taken into account. This problem was later solved by using the Kubo-type formula, where the authors have demonstrated that when the Zeeman fields have been included, some new intra-LL transitions become possible, leading to new quantum Hall plateaus in comparison with the case of lack of these important fields [7]. The importance of spin and valley contributions to Zeeman splitting is also experimentally demonstrated via analyzing the magnetoreflectance spectra in TMDCs monolayer [17] as well as in mono- and multilayer $MoSe_2$ [18]. With the strong spin- and valley-controlled properties and a large natural band gap [19,20], the monolayer WSe_2 [8], and also others of TMDCs materials, display the optical response occurring in the near-infrared region or even in the visible-frequency one, which are completely different from the conventional low-dimensional systems [21] or graphene [22–24].

In parallel with the magnetic field, the role of the electric field has also been of interest in the investigation of transport properties of TMDCs systems [25]. Using the electric field to control the Zeeman-type spin splitting, the authors demonstrated that a tunable exciton splitting in the optical spectra of WSe_2 could be observed experimentally. For the theoretical study, the electric field is also proved to be useful when it has been used to cancel the SOC term in silicene [26] to reduce it as the graphene's value due to the weak SOC in this material.

In the present work we theoretically investigate the effect of out-of-plane magnetic fields on the transport of charge carriers in four different TMDCs: MoS_2, WS_2, $MoSe_2$, and WSe_2. The electronic states are determined by the use of the massive Dirac model. Several scattering mechanisms, encompassing the interaction with impurities, acoustic, and optical phonons, as well as with the substrate surface optical vibration modes, are taken into account. The investigation will also include the presence of an external electric field applied perpendicularly to the monolayers, together with those of spin and valley Zeeman effects. Within such a frame, the main quantity we report on in the study is the magneto-optical absorption coefficient (MOAC) and the full-width at half-maximum (FWHM). While the MOAC is calculated using its relation with the transition probability [27], the FWHM is obtained by a computational calculation. The impurity scattering is considered to have a crucial role and should not be neglected in studying the transport phenomena, especially in the low-temperature range [28]. Therefore, this type of scattering has been used in investigating the magnetoresistivity in graphene [29] and silicene [26], or the conductivity in MoS_2 monolayer [7]. Besides, one of the relevant mechanisms that limit electronic transport in semiconductors is the interaction with lattice vibrations. In the case of TMDCs, both acoustic and optical intrinsic phonon modes participate in the carrier scattering process [30–33]. The interaction with phonon modes pertaining to the substrates on which a given atomic monolayer is formed has also been analyzed both in graphene [34,35] and TMDCs [36] for the case of surface optical phonons. Since to be able to standardize the band gap, the carrier-phonon interaction has been considered to create extra peaks in the optical spectrum [37], and to play a vital role in studying the transport properties of TMDCs [6,32,33]. That is also the reason why the study to determine the information for carriers-phonon interaction, as well as the electronic and phononic dispersion for TMDCs, has been done widely [32,38,39].

To have an overview of the different types of interactions, as well as to point out the predominant characteristics of each material among the four TMDCs systems, in this paper we present the magneto-optical transport properties of different TMDCs materials. Both impurity and phonons scattering, as well as both Zeeman terms and electric field, are considered. The effects of the natural characteristics of materials, external magnetic field, and different substrates on the MOAC and FWHM are presented in detail. A predicted value of the carrier mobility in WS_2, which is inferred from the FWHM data due to intrinsic optical phonon scattering, has been compared and depicted as consistent with experimental observations in the low-temperature region [12].

II. THEORY

A. Basic formalism

We consider a monolayer of TMDCs oriented in the (xy) plane including a magnetic field $\mathbf{B} = (0, 0, B)$. The carriers of the TMDCs system are considered to be scattered by the random impurities combined with the intrinsic phonons in TMDCs as well as with the surface optical (SO) phonons of the substrates. The total Hamiltonian can be written as

$$\mathcal{H} = \mathcal{H}_e + \mathcal{H}_{\rm ph} + \mathcal{H}_{ei} + \mathcal{H}_{ep}. \tag{1}$$

Here, including a perpendicular electric field E_z and two Zeeman terms in the electronic single-particle Hamiltonian of Ref. [10], we obtain

$$\mathcal{H}_e = v_F(\tau\sigma_x\pi_x + \sigma_y\pi_y) + (\Delta_{\tau,s} + d\Delta_z)\sigma_z + O_{\tau,s} + sM_z - \tau M_v. \tag{2}$$

Here v_F is the Fermi velocity, the index $\tau = \pm 1$ stands for valleys K and K', the term $\sigma_{x(y,z)}$ are the Pauli matrices, $2d$ is the vertical distance between the M and X sublattices, $\Delta_z = eE_z$, $\boldsymbol{\pi} = \mathbf{p} + e\mathbf{A}$ is the canonical momentum with $\mathbf{A}$ being the vector potential, Δ is the mass term which plays an important role to create the intrinsic direct energy gap, and the index $s = \pm 1$ refers to spin up and down, respectively. Furthermore, the two terms M_z and M_v have the same form, $M_j = g_j\mu_B B/2$, with $j = z, v$ standing for the spin and valley Zeeman fields, with $\mu_B = e\hbar/2m_e$ referring to the Bohr magneton. Here m_e is the electron effective mass, $g_s = g_e + g'_s$ (with $g_e = 2$ is the free electron g factor [7]) and g_v are the spin and valley Landé g factors. Furthermore, it is noted that the last three terms should be multiplied by a (2×2) identity matrix I_2. The spin- and valley-dependent expressions of Dirac mass $\Delta_{\tau,s}$ and the offset energy $O_{s\tau}$ are given as [1,9,10]

$$\Delta_{\tau,s} = \Delta + \tau s(\lambda_c - \lambda_v)/4, \tag{3}$$

$$O_{\tau,s} = \tau s(\lambda_c + \lambda_v)/4, \tag{4}$$

where λ_c (λ_v) is the conduction (valence) band spin splitting.

Using the Landau gauge $\mathbf{A} = (0, Bx, 0)$ we write the wave function in the form $\psi(\mathbf{r}, k_y) = e^{ik_y y}\psi(x)/\sqrt{L_y}$. Defining the ladder operators which act on the harmonic oscillator wave functions $a_\pm = [\alpha_c/(\hbar\sqrt{2})](\pi_x \pm i\pi_y)$, with $\alpha_c = (\hbar/eB)^{1/2}$, we have $a_+ = (a_-)^\dagger$ and $[a_-, a_+] = 1$. In terms of these

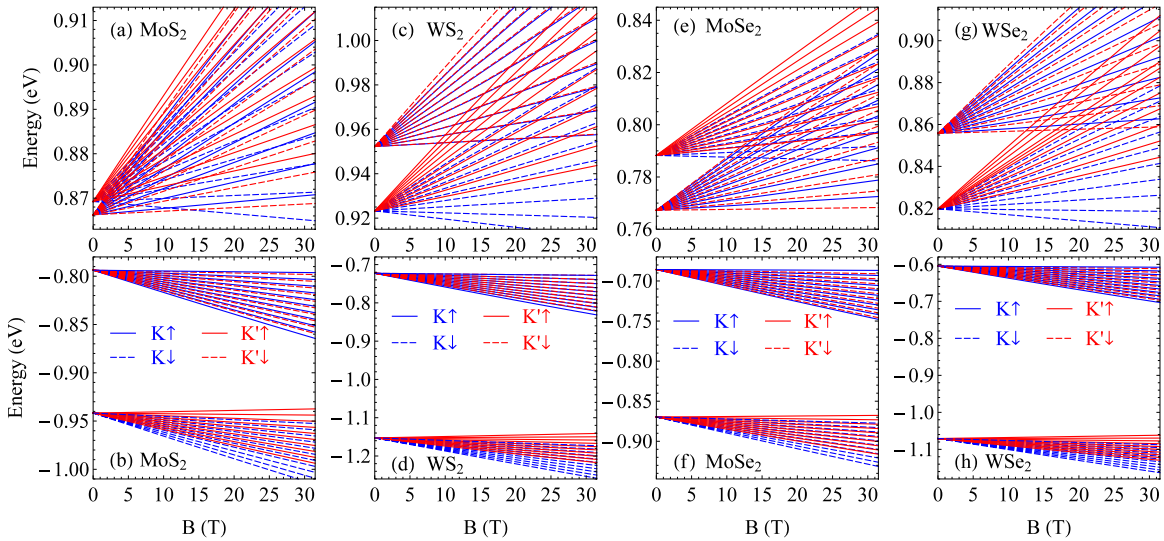

FIG. 1. The LLs of monolayer TMDCs as a function of the magnetic field B including the electric, the spin, and valley Zeeman fields. The applied electric field is $eE_z = 37.75$ meV$/d$. The top [(a), (c), (e), and (g)] and bottom [(b), (d), (f), and (h)] panels correspond to the conduction and valence bands of each material, respectively.

operators the Hamiltonian matrix $\mathcal{H}_e^{\pm}$, with the plus and minus signs pertaining to the K and K' valleys, takes the form

$$\mathcal{H}_e^{\pm} = \begin{pmatrix} \Delta_{\tau,s}^z & \tau\hbar\omega_c a_{\mp} \\ \tau\hbar\omega_c a_{\pm} & -\Delta_{\tau,s}^z \end{pmatrix} + O_{\tau,s} + sM_z - \tau M_v, \quad (5)$$

where $\Delta_{\tau,s}^z = \Delta_{\tau,s} + d\Delta_z$, $\omega_c = v_F\sqrt{2}/\alpha_c$ is the cyclotron frequency. The eigenvalues concerning Eq. (5) for the electronic state $|\alpha\rangle = |n, s, \tau, p\rangle$ are given as follows for the LLs index n ($n \geqslant 1$):

$$E_\alpha = E_{n,s}^{\tau,p} = pE_{n,s}^{\tau,z} + O_{\tau,s} + sM_z - \tau M_v. \quad (6)$$

Here $p = \pm 1$ denotes the conduction and valence band indices, respectively, and $E_{n,s}^{\tau,z} = \{n(\hbar\omega_c)^2 + (\Delta_{\tau,s}^z)^2\}^{1/2}$. Using the fact that $\hbar\omega_c \ll \Delta_{\tau,s}^z$, after expanding the square root in the expression of $E_{n,s}^{\tau}(z)$, we obtain a simpler form for eigenvalues

$$E_{n,s}^{\tau,p} \approx pn\frac{(\hbar\omega_c)^2}{2\Delta_{\tau,s}^z} + p\Delta_{\tau,s}^z + O_{\tau,s} + sM_z - \tau M_v, \quad (7)$$

which displays a usually linear dependence on the LL index and magnetic field of the energy spectrum. The corresponding eigenfunctions $\psi_{n,s}^{\tau,p}(x)$ are

$$\psi_{n,s}^{+1,p}(x) = \begin{pmatrix} A_{n,s}^{+1,p}\phi_{n-1}(x - x_0) \\ B_{n,s}^{+1,p}\phi_n(x - x_0) \end{pmatrix}, \quad (8)$$

$$\psi_{n,s}^{-1,p}(x) = \begin{pmatrix} -A_{n,s}^{-1,p}\phi_n(x - x_0) \\ B_{n,s}^{-1,p}\phi_{n-1}(x - x_0) \end{pmatrix}, \quad (9)$$

where $\phi_n(x - x_0)$ stands for the usual harmonic oscillator wave function, centered at $x_0 = \alpha_c^2 k_y$, and

$$A_{n,s}^{\tau,p} = \left[\frac{pE_{n,s}^{\tau,z} + \Delta_{\tau,s}^z}{2pE_{n,s}^{\tau,z}}\right]^{1/2}, \quad (10)$$

$$B_{n,s}^{\tau,p} = \left[\frac{pE_{n,s}^{\tau,z} - \Delta_{\tau,s}^z}{2pE_{n,s}^{\tau,z}}\right]^{1/2}. \quad (11)$$

The eigenvalues for $n = 0$ are

$$E_{0,s}^{+1} = -(\Delta + d\Delta_z) + s\lambda_v/2 + sM_z - M_v, \quad (12)$$

$$E_{0,s}^{-1} = \Delta + d\Delta_z - s\lambda_c/2 + sM_z + M_v. \quad (13)$$

The associated eigenfunctions for $n = 0$ are given by $\psi_{0,s}^{+1}(x) = (0, \phi_0(x))^T$ and $\psi_{0,s}^{-1}(x) = (\phi_0(x), 0)^T$ with T referring to the transpose. It is noted that for the K (K') valley, its zero level locates in the valence (conduction) band. The eigenfunctions and the zero-level behavior obtained here are reversed with those reported by Tahir *et al.* [7,8] but are in agreement with the results of Wang and Lei [6] for the monolayer MoS_2. However, this difference does not affect the main results when we apply them to evaluate the MOAC.

Figure 1 illustrates the dependence of the eigenvalues in Eqs. (6), (12), and (13) on the magnetic field for finite electric as well as the spin and valley Zeeman fields. For each material, the top (bottom) console refers to the conduction (valence) band. The LLs separation is found to increase linearly with B, agreeing with those reported in previous works [6,7] for MoS_2 material, but in contrast to that in graphene [22,23] and silicene [43] where their LLs depend on the square root of B. This behavior of the LLs spectrum in monolayer TMDCs can be observed from Eq. (7), which is held well because the cyclotron energy $\hbar\omega_c$ is much smaller than $\Delta_{\tau,s}^z$. Besides, we also see that the LLs for both valence and conduction bands are separated into two separate systems due to the spin splitting. It is noted that the spin-splitting feature appears in all materials of TMDCs family, even in the conduction band of monolayer MoS_2, which has not been observed in previous works [6,7]. The reason for this difference is that in previous works, the authors have neglected the term λ_c due to its small value in monolayer MoS_2 (see Table I). If this term is taken into account, as done in the present work, the spin splitting in the conduction band will be equal to $|\tau\lambda_c/2|$, or equal to $|\lambda_c|$ for the total of spin and valley splittings,

TABLE I. List of parameters used in the numerical calculation for different TDMCs. Values of $\hbar v_F$ (eV Å) and Δ (eV) are taken from Ref. [40], λ_v (eV) and λ_c (eV) are from Ref. [41], and g_s' and g_v are from Ref. [42].

	$\hbar v_F$	Δ	λ_v	λ_c	g_s'	g_v
MoS_2	3.51	0.83	0.148	−0.003	0.21	3.57
WS_2	4.38	0.90	0.430	+0.029	0.84	4.96
$MoSe_2$	3.11	0.74	0.184	−0.021	0.29	3.03
WSe_2	3.94	0.80	0.466	+0.036	0.98	4.34

at $B = 0$. Furthermore, Figs. 1(a), 1(c), 1(e), and 1(g) show that with the biggest value of $|\lambda_c|$, WSe_2 displays the largest spin splitting in the conduction band while MoS_2 shows the smallest. Besides, because the values of λ_c in MoS_2 and $MoSe_2$ are negative, the conduction LLs for the spin-up case of K' valleys in these two materials have higher values than those of K valleys. An opposite result is observed in WS_2 and WSe_2 due to their positive λ_c values.

To have a more visual view of the influence of electric and Zeeman fields on the LLs spectrum, in Fig. 2 we describe the LLs (conduction band) versus the magnetic field for two cases. In the case of $M_z = 0$, $M_v = 0$, and $eE_z = 37.75$ meV$/d$ (the left panel) our result reduces to that reported in previous work [6] which showed a reverse feature of the LLs spectrum for the spin up and down between the K and K' valleys, i.e., $K\uparrow = K'\downarrow$ and $K\downarrow = K'\uparrow$. Besides the spin splitting due to the finite value of λ_c as mentioned above, the other difference between ours and previous results is the values of LLs where the electric field has pushed the LLs up to the higher values in our result in comparison with that of Wang and Lei [6]. Meanwhile, in the case of $M_z \neq 0$, $M_v \neq 0$, and $E_z = 0$ [see Fig. 2(b)] our result is the same as that of Tahir *et al.* [7] where the spin and valley Zeeman fields have been included but the electric field has not. The only different thing between them is the spin-splitting behavior which has not been observed in previous work due to neglecting the term λ_c. This reveals that the combined strong SOC and Zeeman fields have doubled LLs but have not changed the energy gap of monolayer TMDCs while the effect of the electric field depends on its direction. With the direction shown in Hamiltonian (2) the electric field increases the energy gap, but if we reverse the electric direction then the energy gap would

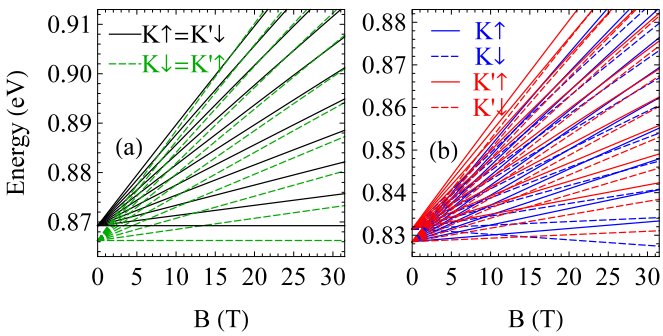

FIG. 2. The LLs of monolayer MoS_2 (conduction band) versus the magnetic field B. (a) $M_z = M_v = 0$ and $eE_z = 37.75$ meV$/d$, while (b) is for $M_z \neq 0$, $M_v \neq 0$, and $E_z = 0$.

be decreased. This feature has also been observed in other 2D materials such as silicene [26,44], GaN [45], and $SnSe_2$ [46].

In Eq. (1), the term $\mathcal{H}_{\rm ph}$ denotes the phononic part of Hamiltonian, which is given as follows:

$$\mathcal{H}_{\rm ph} = \sum_{\mathbf{q},\nu} \hbar\omega_{\mathbf{q},\nu} b^\dagger_{\mathbf{q},\nu} b_{\mathbf{q},\nu}, \tag{14}$$

where $b^\dagger_{\mathbf{q},\nu}$ ($b_{\mathbf{q},\nu}$) denotes the phonon creation (annihilation) operator with frequency $\omega_{\mathbf{q},\nu}$ of the 2D wave vector $\mathbf{q}$ and branch ν. The last two terms of Eq. (1) are the carrier-impurity and carrier-phonon parts of the Hamiltonian, which have the following forms [6]:

$$\mathcal{H}_{ei} = \sum_{\mathbf{q},a} \sum_{\alpha,\alpha'} U(q) J_{\alpha,\alpha'}(q) e^{i\mathbf{q}(\mathbf{r}-\mathbf{r}_a)} c^\dagger_\alpha c_{\alpha'}, \tag{15}$$

$$\mathcal{H}_{ep} = \sum_{\mathbf{q},\nu} \sum_{\alpha,\alpha'} g^\nu_{\mathbf{q}} J_{\alpha,\alpha'}(q) e^{i\mathbf{q}\mathbf{r}} c^\dagger_\alpha c_{\alpha'} (b^\dagger_{-\mathbf{q},\nu} + b_{\mathbf{q},\nu}). \tag{16}$$

Here $U(q)$ is the carrier-impurity scattering potential at the impurity position $\mathbf{r}_a$, furthermore, $g^\nu_{\mathbf{q}}$ is the carrier-phonon coupling matrix depending on the phonon mode ν, and $c^\dagger_\alpha$ ($c_{\alpha'}$) refers to the carrier creation (annihilation) operator at α state. The form factor is given as follows:

$$J_{\alpha,\alpha'}(q) = \int_{-\infty}^{+\infty} e^{iq_x x} dx \left[\psi^{\tau',p'}_{n',s'}(x)\right]^\dagger \psi^{\tau,p}_{n,s}(x), \tag{17}$$

whose detailed expression is presented in Appendix A.

B. Magneto-optical absorption coefficient

The MOAC is calculated using its relation with the transition probability as follows [27]:

$$K^\beta(\Omega) = \frac{1}{V_0 N_\Omega} \sum_{\alpha,\alpha'} \mathcal{W}^{\beta,\pm}_{\alpha',\alpha} f_\alpha (1 - f_{\alpha'}). \tag{18}$$

Here $\beta = i, \nu$ for impurity and phonon (of ν mode) scatterings, respectively, V_0 is the sample volume, N_Ω is the incident photon density of energy $\hbar\Omega$, and $f_{\alpha(\alpha')}$ is the Fermi distribution function. The transition matrix element for impurity and phonon scattering can be formally expressed in the same form by the second-order Born golden rule, in which the ℓ-photon absorption process has been taken into account [47,48]:

$$\mathcal{W}^{\beta,\pm}_{\alpha',\alpha} = \frac{2\pi}{\hbar^3\Omega^2} \sum_{\alpha'',\mathbf{q}} \sum_{\ell=1}^{\infty} \left|\mathcal{M}^{\beta,\pm}_{\alpha',\alpha''}\right|^2 \left|\mathcal{M}^{\rm rad}_{\alpha'',\alpha}\right|^2 \times \frac{(\alpha_0 q)^{2\ell}}{(\ell!)^2 2^{2\ell}} \delta\left(E_{\alpha'} - E_\alpha \pm \hbar\omega^\beta_{\mathbf{q}} - \ell\hbar\Omega\right). \tag{19}$$

Here $\hbar\omega^\beta_{\mathbf{q}} = 0$ and/or $\hbar\omega^\beta_{\mathbf{q}} = \hbar\omega^\nu_{\mathbf{q}}$ are for impurity and/or phonon scattering, respectively, the plus (minus) sign in Eq. (19) stands for the emission (absorption) process of a phonon with energy $\hbar\omega^\nu_{\mathbf{q}}$. Furthermore, $\alpha_0 = 7$ nm is the dressing parameter [27,49]. In the case of carrier-phonon scattering, the matrix element in Eq. (19) describes the three particles interaction. Its physical meaning is as follows: The carriers in initial state $|\alpha\rangle$ first absorb ℓ photons to make a transition to the intermediate one $|\alpha''\rangle$, and then emit or absorb one phonon to jump to the final state $|\alpha'\rangle$. In more detail, the carrier-impurity and carrier-phonon matrix elements are given

by

$$\left|\mathcal{M}^{\beta,\pm}_{\alpha',\alpha''}\right|^2 = N^{\beta,\pm}_{\mathbf{q}}\left|\mathrm{g}^{\beta}_{\mathbf{q}}\right|^2\cos^2\left(\frac{\theta}{2}\right)|J_{\alpha',\alpha''}(q)|^2\delta_{s',s''}\delta_{k''_y,k'_y\mp q_y}, \quad (20)$$

where $N^{\beta,\pm}_{\mathbf{q}} = n_i$ for the case of impurity scattering with $n_i = 1\times10^{13}$ m^{-2} being the impurity density [7], while it is $N^{\beta,\pm}_{\mathbf{q}} = N^{\nu,\pm}_{\mathbf{q}} = N^{\nu}_{\mathbf{q}} + 0.5 \pm 0.5$ for the case of phonon scattering with $N^{\nu}_{\mathbf{q}}$ being the Bose distribution function for the phonon mode index ν, and θ is the scattering angle. Furthermore, $\mathrm{g}^{\beta}_{\mathbf{q}} = U(q)$ and/or $\mathrm{g}^{\beta}_{\mathbf{q}} = \mathrm{g}^{\nu}_{\mathbf{q}}$ for impurity and/or phonon scattering, respectively. Using Eq. (17) and the eigenfunctions (8) and (9), the form factor is given as follows for the intravalley ($\tau' = \tau'' = \tau$) transition (see Appendix A):

$$|J_{\alpha',\alpha''}(q)|^2 = e^{-u}u^j\frac{k!}{(k+j)!}\left[B^{\tau,p'}_{n',s'}B^{\tau,p''}_{n'',s''}L^j_k(u) + A^{\tau,p'}_{n',s'}A^{\tau,p''}_{n'',s''}\sqrt{\frac{k+j}{k}}L^j_{k-1}(u)\right]^2, \quad (21)$$

where we have used the denotations $u = \alpha_c^2q^2/2$, the symbol k is $k = \min[n', n'']$, $j = |n'' - n'|$, and $L^j_k(u)$ stands for the associated Laguerre polynomials. In Eq. (19), the carrier-photon interaction part of the matrix element is given by [50]

$$\left|\mathcal{M}^{\mathrm{rad}}_{\alpha'',\alpha}\right|^2 = \frac{\Omega^2A_0^2}{4}|\mathbf{e}_{\mathrm{rad}}\cdot e\mathcal{B}_{\alpha''\alpha}|^2, \quad (22)$$

where A_0 is the amplitude of the vector potential and $\mathbf{e}_{\mathrm{rad}}$ refers to the radiation polarization vector assumed to be polarized along the x direction, and the dipole moment $e\mathcal{B}_{\alpha''\alpha} = e\langle\alpha''|\mathbf{r}|\alpha\rangle$ is calculated as follows:

$$e\mathcal{B}_{\alpha''\alpha} = e\delta_{s'',s}\delta_{k''_y,k_y}\left[A^{\tau'',p''}_{n'',s''}A^{\tau,p}_{n,s} + B^{\tau'',p''}_{n'',s''}B^{\tau,p}_{n,s}\right] \times\left[x_0\delta_{n'',n} + \frac{\alpha_c}{\sqrt{2}}(\sqrt{n}\delta_{n'',n-1} + \sqrt{n+1}\delta_{n'',n+1})\right]. \quad (23)$$

It shows that the transitions occur in the monolayer of TMDCs when the LLs index is unchanged ($\Delta n = 0$) or changes only one unit $\Delta n = \pm1$. This is similar to that in graphene [49,51] and silicene [26,43].

Using the above results, the general expression for the MOAC due to carrier-impurity and carrier-phonon scattering is found as follows:

$$K^{\beta}(\Omega) = \sum_{\alpha,\alpha',\alpha''}G(\alpha)\int_0^{\infty}dq\,q^3\left|\mathrm{g}^{\beta}_{\mathbf{q}}\right|^2|J_{\alpha',\alpha''}(q)|^2 \times\left\{N^{\beta,\pm}_{\mathbf{q}}\delta\left(X^{\beta,\pm}_1\right) + \frac{\alpha_0^2q^2}{16}N^{\beta,\pm}_{\mathbf{q}}\delta\left(X^{\beta,\pm}_2\right)\right\}, \quad (24)$$

where the results are calculated up to the two-photon process. Furthermore, we have denoted

$$G(\alpha) = \frac{d_sd_vS_0e^2\alpha_0^2}{64\pi n_rc\varepsilon_0\hbar^2\Omega\alpha_c^2}|\mathcal{B}_{\alpha''\alpha}|^2f_{\alpha}(1-f_{\alpha'}), \quad (25)$$

$$\mathcal{X}^{\beta,\pm}_{\ell} = E_{\alpha'} - E_{\alpha} \pm \hbar\omega^{\beta}_{\mathbf{q}} - \ell\hbar\Omega \quad (\ell = 1, 2). \quad (26)$$

Here $d_s = 1$ ($d_v = 1$) is the spin (valley) degeneracy, $S_0 = V_0/h$ is the sample area with h being the layer thickness, n_r is the material refractive index, c is the light speed, and ε_0 is the vacuum permittivity. The expression in Eq. (24) is obtained for the general case, which can be used to evaluate different types of scatterings such as impurity, acoustic, optical, and SO phonons. The following results are calculated for the carrier density $n_c = 1.35\times10^{13}$ cm^{-2} [11] which leads to the Fermi energies of 228.6, 285.2, 202.5, and 256.6 meV for MoS_2, WS_2, $MoSe_2$, and WSe_2, respectively, which are inferred from the formula $\varepsilon_{\mathrm{F}} = \hbar v_F(\pi n_c)^{1/2}$ [29]. Note that the Fermi level is found to depend on E_{α} [7,8], i.e., ε_{F} depends on the external magnetic and electric fields. However, we assume the above approximation of the Fermi level still holds good, as it is successfully employed in magnetotransport study in graphene [29]. These values of the Fermi level give their locations in the middle of conduction and valence bands. Therefore, the carriers of this study are electrons, and all allowed transitions are the inter-LL transitions. There is no intra-LL transition allowed, and the first inter-LL transition arises from the highest LL of the valence band to the lowest LL of the conduction band. Besides, due to the similarities between K and K' valleys, in the following, we would only focus on the K valley and put $\tau = \tau' = 1$ as an input data in all calculations, but the results could be also validated for the K' valley.

III. RESULTS AND DISCUSSION

A. Impurity scattering

For the carrier-impurity interaction, its intravalley scattering potential is given as follows [7,52]:

$$U(q) = \frac{U_0}{\left(q^2 + k_s^2\right)^{1/2}}, \quad (27)$$

where $U_0 = e^2/(2S_0\varepsilon_0\varepsilon_r)$ and $k_s = e^2\sqrt{n_e}/(\sqrt{\pi}\varepsilon_0\varepsilon_r\hbar v_F)$ is the screening wave vector [53] with $\varepsilon_r = (\varepsilon_{\perp}\varepsilon_{\parallel})^{1/2}$ being the relative permittivity of TDMCs. In the case of short-ranged potential, the scattering potential reduces to $U(\mathbf{q}) \approx U_0/k_s$ due to the approximation $q \ll k_s$. Inserting Eq. (27) into Eq. (24), the MOAC for carrier-impurity scattering is found to be

$$K^i(\Omega) = \frac{4n_iU_0^2}{k_s^2\alpha_c^4}\sum_{\alpha,\alpha',\alpha''}G(\alpha)\left\{\mathcal{Q}^{(1)}_{\alpha',\alpha''}\delta\left(X^i_1\right) + \frac{\alpha_0^2}{8\alpha_c^2}\mathcal{Q}^{(2)}_{\alpha',\alpha''}\delta\left(X^i_2\right)\right\}, \quad (28)$$

where we have introduced the dimensionless integral

$$\mathcal{Q}^{(\ell)}_{\alpha',\alpha''} = \int_0^{\infty}u^{\ell}|J_{\alpha',\alpha''}(u)|^2du, \quad (29)$$

which could be analytically calculated for the ℓ-photon absorption process by using Eqs. (A1)–(A4) of Ref. [51] (see Appendix B). The arguments of delta functions in Eq. (28) are $X^i_{\ell} = E_{\alpha'} - E_{\alpha} - \ell\hbar\Omega$, $\ell = 1, 2$. According to the collision-broadening model [54], these delta functions would be replaced by the Lorentzians of the widths $(\Gamma^i_{\alpha,\alpha'})^2 = (S_0U_0^2/2\pi k_s^2\alpha_c^2)\mathcal{Q}^{(0)}_{\alpha',\alpha''}\delta_{s,s'}$, where $\mathcal{Q}^{(0)}_{\alpha',\alpha''}$ is given in Eq. (29) for $\ell = 0$.

In Fig. 3 we show the dependence of MOAC in MoS_2 due to carrier-impurity scattering on the photon energy at $B = 10$ T

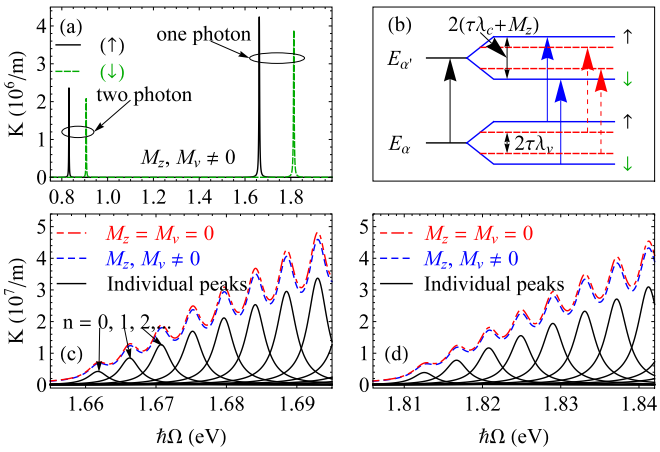

FIG. 3. The MOAC in monolayer MoS_2 versus photon energy including the electric, the spin, and valley Zeeman fields: (a) Transition from $n = 0$ to $n' = 1$, (b) the diagram transition and spin separation, (c) transitions between different LLs for spin up, and (d) the same as those in (c) but for spin down. The results are evaluated at $B = 10$ T, $T = 4$ K, and $eE_z = 37.75$ meV/d.

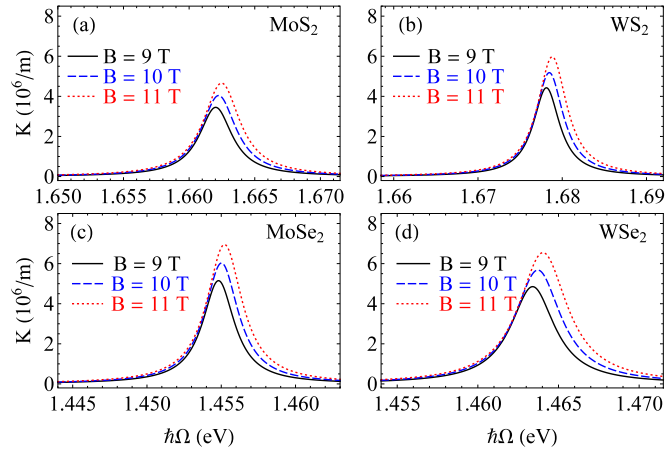

FIG. 4. The MOAC caused by the first transition (from $n = 0$ to $n' = 1$) in monolayer TMDCs versus photon energy for different magnetic fields at $T = 4$ K, $e\Delta_z = 37.75$ meV/d, and M_z, $M_v \neq 0$.

and $eE_z = 37.75$ meV/d, using parameters in Table II. This electric field value is chosen to cancel the SOC term in MoS_2 for the case of $\tau s = +1$, i.e., in the $K\uparrow$ or $K'\downarrow$. Figure 3(a) depicts the first individual transition for both cases of spin up and down as well as for both one- and two-photon processes. It is seen that in both spin-up and spin-down cases, the one-photon absorption peaks are located in the visible region, which is resulting from the large band gap of MoS_2 and other TMDCs as well. This behavior is also observed for the optical conductivity in monolayer WSe_2 [8,57], but is different from that in graphene [22] and other graphenelike 2D systems [43,58,59]. Another noteworthy result is the splitting of the MOAC peaks caused by the spin up and down. This is caused by the strong SOC in MoS_2. Besides, with the stronger spin-splitting effect, the spin-down absorption peaks are always located on the right-hand side of the spin-up ones in both one- and two-photon absorption cases. Moreover, the bigger absorbed photon energies here, in comparison with those in previous works [27], illustrates that the energy gap of MoS_2 is expanded when the electric, as well as the Zeeman fields, are applied to the system. We also see from Fig. 3(a) that the ratio between the peak values due to the two- and one-photon processes is about 55.8% in both spin-up and spin-down cases. This value is slightly higher than that in the absence of the electric and Zeeman fields effect [27], once again showing a notable contribution of the two-photon process in comparison with the one-photon process, and should be included in studying the transport properties of monolayer TMDCs.

TABLE II. List of parameters used in the numerical calculation for different TDMCs. Values of a (Å) is taken from Ref. [40], n_r is from Ref. [55], $\varepsilon_\perp$ and $\varepsilon_\parallel$ are from Ref. [56], and m_e (m_0) is from Ref. [42].

	a	n_r	$\varepsilon_\perp$	$\varepsilon_\parallel$	m_e
MoS_2	3.193	6.50	6.4	15.3	0.49
WS_2	3.197	6.25	6.3	13.7	0.35
$MoSe_2$	3.313	4.25	7.4	17.1	0.64
WSe_2	3.310	5.68	7.5	15.3	0.40

Figures 3(c) and 3(d) illustrate the transitions between different LLs in monolayer MoS_2, for example, for the cases of spin up and down, respectively. While the black solid lines show the individual peaks (which arise from the transition from an individual LL to another one) the blue dashed and the red dashed-dotted lines show the total transition. It is clear that the Zeeman fields do not affect the positions of the peaks but slightly reduce their intensities. This reveals that when the Zeeman fields are included, although each LL is shifted with a value of M_z caused by spin splitting, the LLs spacings do not change. Therefore, unlike in a previous work [7], where the Fermi level is completely in the conduction band, allowing some intra-LL transitions could have occurred, the combined effect of SOC, Zeeman fields, and magnetic fields would have raised new intra-LL transitions, this combined effect does not allow any new inter-LL transitions. This feature can be observed clearly from the transition diagram in Fig. 3(b). In the absence of Zeeman fields (labeled by the red dashed lines) due to the spin splitting, each LL is shifted by a value of $\tau\lambda_{c/v}$, while this value is $(\tau\lambda_{c/v} + M_z)$ in the presence of Zeeman fields. However, we can observe in Fig. 3(b) that the energy separations in both cases are equal. This is due to the fact that with a case of spin up and/or down, each LL is added by the same value, therefore, their separation is unchanged with the Zeeman fields effect in both cases spin up and down. In the following, we present only for the spin-up case, but the result would be also valid for the spin down as well.

To understand the effect of magnetic field on the optical transport properties of monolayer TMDCs, in Fig. 4 we show the MOAC caused by the first transition versus photon energy with the B value changing from 9 to 11 T. Each panel in Fig. 4 describes the third peak in Fig. 3(a) in detail for three B values. The absorbed photon energies here satisfy the resonant condition

$$\ell\hbar\Omega = E^{+1,+1}_{1,+1} - E^{+1}_{0,+1}, \tag{30}$$

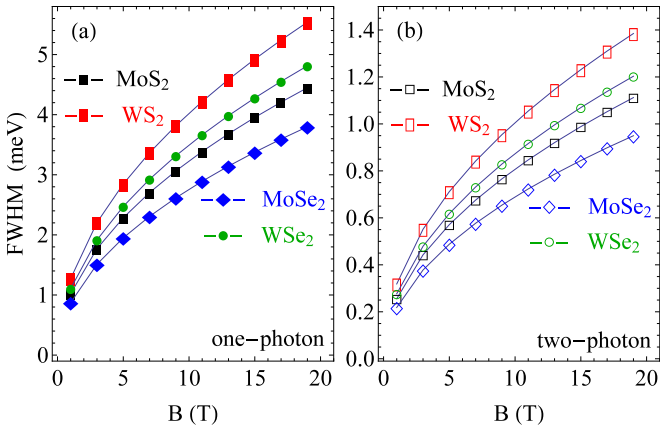

FIG. 5. The FWHM of the peaks shown in Fig. 4 versus the magnetic field. The left (a) and right (b) consoles are for the one- and two-photon processes, respectively.

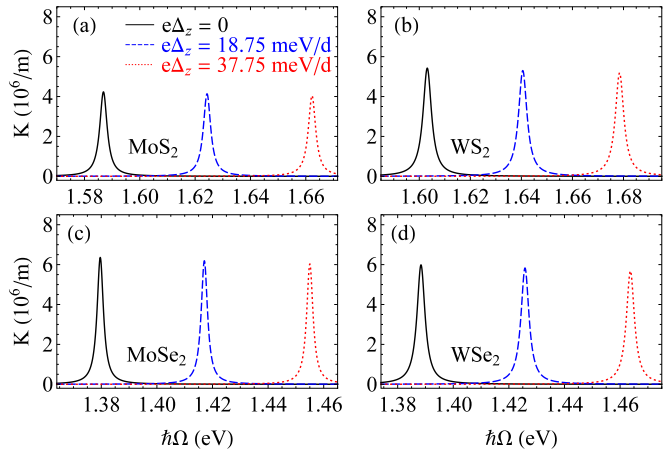

FIG. 6. The MOAC due to the first transition in monolayer TMDCs versus photon energy for different electric fields at $B = 10$ T, $T = 4$ K, and $M_z, M_v \neq 0$.

with $\ell = 1$ (one photon). For example, for each value of B of 9, 10, and 11 T, the MOAC spectrum for monolayer MoS_2 [Fig. 4(a)] shows a single peak at $\hbar\Omega = 1.66202$, 1.66225, and 1.66247 eV, respectively. It is clear to observe a blueshift in the MOAC peaks with the increase of the magnetic field. This feature results from the expanding of the LL spacing, $E^{+1,+1}_{1,+1} - E^{+1}_{0,+1}$, when the magnetic field increases. This result is similar to that in traditional low-dimensional systems [21] and graphene [24,35]. The increase of peak intensities comes from the reduction of magnetic length α_c with the magnetic field. This can be analytically explained from Eq. (28) where $K^i(\Omega) \sim \alpha_c^{-4} \sim B^2$. Physically, this is the cause of a well-known phenomenon that the stronger magnetic field leads to a stronger carrier-impurity interaction. Besides, with the largest value of Δ the WS_2 displays the largest values of the absorbed photon energies while the $MoSe_2$ shows the smallest one. Meanwhile, the MOAC intensities for different materials are almost of the same order.

In addition to the position and intensity, the FWHM is also an important feature of the resonant peak. In Fig. 5 we show the FWHM of the first transition peak as a function of B. The main trend observed is a significant increase in the FWHM when the magnetic field increases for both one- and two-photon processes as well as for all four materials. Because of the close relationship between FWHM and Lorentzian width, the $\sqrt{B}$-dependent FWHM is explained from the relation that $\Gamma^i_{\alpha,\alpha'} \sim \alpha_c^{-1} \sim B^{1/2}$. This is in agreement with the broadening LLs model [60] and the previous observation in graphene [49,51,61]. Physically, when the magnetic field becomes stronger, the quantum confinement effect will be enhanced, resulting in an increase of the carrier-impurity scattering, and so does the FWHM. We now study the effect of different materials on the FWHM. It can be seen from the Lorentzian formula that the different materials affect the FWHM mainly through their values of the ratio v_F^2/S_0. With its biggest value of this ratio, WS_2 displays the largest FWHM while $MoSe_2$ shows the smallest FWHM among the four. This reveals that the carrier-impurity interaction in WS_2 is the strongest.

In order to observe the electric field effect, in Fig. 6 we show the MOAC as a function of photon energy for different values of the electric field while retaining the magnetic field at $B = 10$ T. When the electric field increases the absorption spectrum shifts to the higher energy range and almost remains constant in its intensity. This reveals that the electric field increases the band gap of TDMCs but hardly affects the absorption spectrum intensity.

B. Intrinsic acoustic and optical phonons scattering

For phonon scatterings, a particularly useful model is the deformation potential approximation, in which the scattering potential is simplified by the expression in the zeroth order and the first order of the phonon momentum for the optical and acoustic phonons, respectively [39]. Therefore, the carrier-phonon coupling matrix element for both acoustic and optical phonon can be treated in the same form as follows [32,33,62]:

$$\left|g^{\nu}_{\mathbf{q}}\right|^2 = \frac{\hbar}{2S_0\rho\omega^{\nu}_{\mathbf{q}}}\left|D^{\nu}_{\mathbf{q}}\right|^2, \tag{31}$$

where ρ is the mass density. Furthermore, $D^{\nu}_{\mathbf{q}}$ is the electron-phonon coupling strength, which is dependent on the phonon mode ν, i.e., $D^{\rm ac}_{\mathbf{q}} = (D_1 q)$ for acoustic phonon and $D^{\rm op}_{\mathbf{q}} = D_0$ for optical phonon, respectively.

For the acoustic phonon, we use the linear dispersion $\omega^{\rm ac}_{\mathbf{q}} = v_s q$, where v_s is the sound velocity. Due to their very small values, the acoustic phonon energies in the delta functions of Eq. (24) are neglected in comparison with the separation energies $(E_{\alpha'} - E_{\alpha})$. Using this assumption into Eq. (24) we will obtain the following expression for quasielastic scattering by deformation potential acoustic phonon:

$$K^{\rm ac}(\Omega) = \frac{2k_BTD_1^2}{V_0\rho v_s^2\alpha_c^4}\sum_{\alpha,\alpha'\alpha''} G(\alpha)\Big\{\mathcal{Q}^{(1)}_{\alpha',\alpha''}\delta\big(X^{\rm ac}_1\big) + \frac{\alpha_0^2}{8\alpha_c^2}\mathcal{Q}^{(2)}_{\alpha',\alpha''}\delta\big(X^{\rm ac}_2\big)\Big\}, \tag{32}$$

where the dimensionless integrals $\mathcal{Q}^{(1,2)}_{\alpha',\alpha''}$ are defined in Eqs. (B1) and (B2) and $X^{\rm ac}_{\ell} = X^i_{\ell}$. The corresponding Lorentzian width for the case of acoustic phonon scattering is $(\Gamma^{\rm ac}_{\alpha,\alpha'})^2 = (D_1^2k_BT/4\pi\rho v_s^2\alpha_c^2)\mathcal{Q}^{(0)}_{\alpha',\alpha''}\delta_{s,s'}$, where $\mathcal{Q}^{(0)}_{\alpha',\alpha''}$ is given in Eq. (29) for $\ell = 0$.

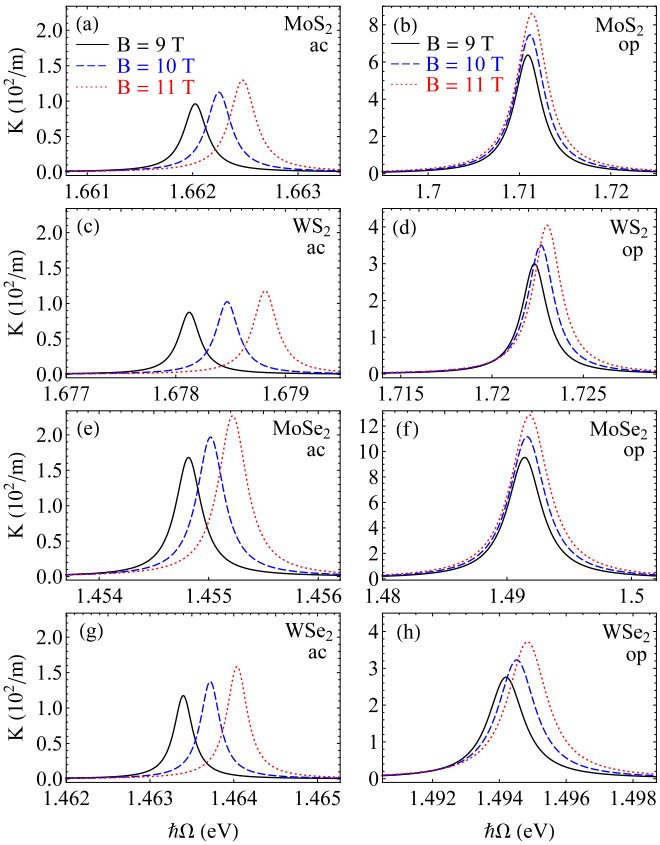

FIG. 7. The MOAC in monolayer TMDCs due to acoustic and optical phonon scattering is shown as a function of photon energy for different magnetic fields. The results are evaluated at $T = 4$ K, $e\Delta_z = 37.75$ meV$/d$, and $M_z, M_v \neq 0$. Symbols "ac" and "op" refer to the acoustic and optical phonons scattering, respectively.

For the intrinsic optical phonon scattering, using its dispersionless frequency $\omega_{\mathbf{q}}^{\rm op} = \omega_{\rm op}$ the expression for MOAC is found as follows:

$$K^{\rm op}(\Omega) = \frac{\hbar D_0^2}{V_0 \rho \omega_{\rm op} \alpha_c^4} \sum_{\alpha,\alpha'\alpha''} G(\alpha) \Big\{ \mathcal{Q}^{(1)}_{\alpha',\alpha''} \big[N_{\mathbf{q}}^{\rm op,-} \delta\big(X_1^{\rm op,-}\big) + N_{\mathbf{q}}^{\rm op,+} \delta\big(X_1^{\rm op,+}\big)\big] + \frac{\alpha_0^2}{8\alpha_c^2} \mathcal{Q}^{(2)}_{\alpha',\alpha''} \times \big[N_{\mathbf{q}}^{\rm op,-} \delta\big(X_2^{\rm op,-}\big) + N_{\mathbf{q}}^{\rm op,+} \delta\big(X_2^{\rm op,+}\big)\big] \Big\}, \tag{33}$$

where $N_{\mathbf{q}}^{\rm op,\pm} = N_{\mathbf{q}}^{\rm op} + 1/2 \pm 1/2$ with $N_{\mathbf{q}}^{\rm op}$ being the distribution function for optical phonon, $\mathcal{Q}^{(\ell)}_{\alpha',\alpha''}$ is defined in Eq. (29), and

$$X_\ell^{\rm op,\pm} = E_{\alpha'} - E_\alpha \pm \hbar\omega_{\rm op} - \ell\hbar\Omega. \tag{34}$$

The Lorentzian width for optical phonon scattering is $(\Gamma^{\pm,{\rm op}}_{\alpha,\alpha'})^2 = (\hbar D_0^2/4\pi\rho\omega_{\rm op}\alpha_c^2)\mathcal{Q}^{(0)}_{\alpha',\alpha''} N_{\mathbf{q}}^{\rm op,\pm} \delta_{s,s'}$, which is dependent on the LLs.

To study the influence of magnetic field on the transport properties of the monolayer of TMDCs, in Fig. 7 we present the MOAC versus photon energy for three values of magnetic fields using parameters in Table III. Similar to the impurity scattering case, here we also observe that the magnetic field increases the MOAC intensity and pushes its peaks positions to the higher region. However, the MOAC intensities in both acoustic and optical phonons scattering are much smaller than those in the impurity scattering with a ratio being of the order of 10^4 times (10^6/m versus 10^2/m). This reveals that at the low temperature the impurity scattering plays a dominant role in comparison to the phonons, being in good agreement with previous theoretical [28] and experimental [65] studies in semiconductors.

TABLE III. List of parameters used in the numerical calculation for different TDMCs. The values of D_0 (10^8 eV/cm), D_1 (eV), and $\hbar\omega_{\rm op}$ (meV) are taken from Ref. [39], the values of ρ ($\times 10^{-7}$ g/cm^2) and v_s ($\times 10^5$ cm/s) are taken from Ref. [63], and the value of $h = 2d$ (Å) is taken from Ref. [38].

	D_0	D_1	ρ	v_s	$\hbar\omega_{\rm op}$	h
MoS_2	5.8	4.5	1.56	6.6	48.9[a]	3.13
WS_2	3.1	3.2	2.36	4.3	44.2	3.14
$MoSe_2$	5.2	3.4	2.01	4.1	36.6	3.35
WSe_2	2.3	3.2	3.09	3.3	30.8	3.36

[a]Reference [64].

In comparison with the optical phonon scattering case, the MOAC intensity due to acoustic one has the same order but with about 2–6 times smaller values. Besides, since the acoustic phonon energy is ignored in the delta functions of Eq. (24) caused by its small value, its scattering peak positions located in the same position as those due to the impurity scattering. Meanwhile, the peak positions due to optical phonon scattering shift to the higher energy region due to their finite values of the optical phonon energies. The absorbed photon energies in the case of optical phonon interaction satisfy the resonant condition

$$\ell\hbar\Omega = E_{1,+1}^{+1,+1} - E_{0,+1}^{+1} + \hbar\omega_{\rm op}, \tag{35}$$

with $\ell = 1$ (one-photon process). It is clear that with the biggest optical phonon energy (see Table III), MoS_2 displays the largest shift (comparison with the peaks due to acoustic phonon interaction) while the WSe_2 depicts the smallest shift among the four materials. Moreover, the effect of different TMDC materials on the MOAC intensity is mainly decided by the ratios $D_1^2/(n_r h\rho v_s^2)$ and $D_0^2/(n_r h\rho\omega_{\rm op})$ for acoustic and optical phonons scattering, respectively [see Eqs. (32) and (33)]. With the biggest value of these ratios, the $MoSe_2$ has the biggest MOAC intensities in both acoustic and optical phonon interaction cases, while WS_2 shows the smallest ones. This is the same in the case of impurity as shown in Fig. 4. Therefore, in general, the relative values of MOAC intensity depend on the characteristics of materials, but does not depend on the interaction mechanism.

In Fig. 8 we illustrate the FWHM of resonant peaks shown in Fig. 7 as a function of B. Similar to the impurity scattering case, an almost $\sqrt{B}$ dependence of FWHM has also been observed in the case of phonon scattering. This is because the Lorentzian widths in all these mechanisms are proportional to $\alpha_c^{-1} \sim B^{1/2}$. Moreover, from the expressions of the Lorentzian widths, the effect of different TMDC materials on the FWHM is mainly decided by the ratios $D_1^2/(\rho v_s^2)$ and $D_0^2/(\rho\omega_{\rm op})$ for acoustic and optical phonons scattering, respectively. For

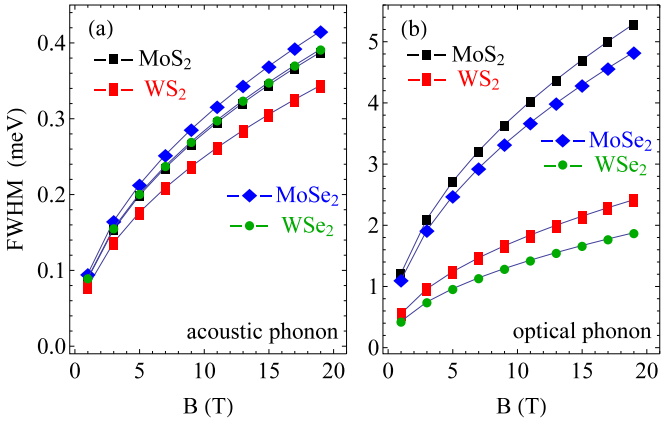

FIG. 8. The FWHM of the peaks shown in Fig. 7 as a function of magnetic field.

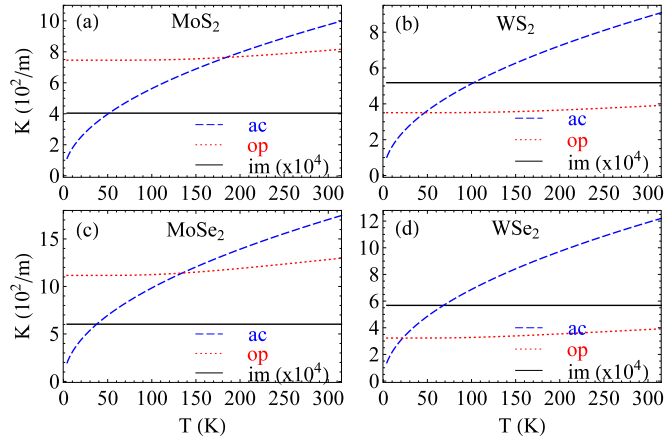

FIG. 9. Temperature dependence of the peak value of MOAC at $\hbar\Omega = E^{+1,+1}_{1,+1} - E^{+1}_{0,+1} + \hbar\omega^{\beta}_{\mathbf{q}}$. The results are evaluated for one-photon process, at $e\Delta_z = 37.75$ meV$/d$, $M_z, M_v \neq 0$, and $B = 10$ T. Symbols ac, op, and im refer to the acoustic phonon, optical phonon, and impurity scattering, respectively (note the factor of 10^4 in the case of impurity scattering).

the acoustic phonon interaction, with the largest value of $D_1^2/(\rho v_s^2)$, $MoSe_2$ displays the biggest FWHM while the WS_2 exhibits the smallest one. On the other hand, for the optical phonon scattering, MoS_2 depicts the biggest FWHM due to its biggest ratio of $D_0^2/(\rho\omega_{\rm op})$, while WSe_2 has the smallest FWHM among the four materials. Therefore, we can conclude from Figs. 5 and 8 that the FWHM depends not only on the parameters of materials but also on the interaction mechanism.

Another interesting feature of the FWHM is its usefulness in predicting the carrier mobilities. From the FWHM data in Fig. 8 using the expression of Landau-level broadening in the vicinity of Fermi energy [29]

$$\Gamma(B) = \frac{ev_F}{\pi}\sqrt{\frac{2\alpha_\Gamma B}{n_c\mu_0}}, \tag{36}$$

with a suitable value of the broadening parameter α_Γ, we can predict the carrier mobility values μ_0 in the monolayer TMDCs. The value of α_Γ can be found by fitting the FWHM data and available experimental value of mobility. For example, using the value of mobility of 174 $cm^2/(V\ s)$, which was experimentally observed at 4 K in monolayer MoS_2 [11], we obtain $\alpha_\Gamma = 8.1\times10^{-5}$ (1.5×10^{-2}), for the acoustic (optical) phonon scattering. Then using these results of α_Γ into Eq. (36) we can predict the phonon limited mobility in other monolayer TMDCs as follows: 344.8 (129.3), 119.1 (163.3), and 215.2 (173.4) $cm^2/(V\ s)$ for WS_2, $MoSe_2$, and WSe_2, respectively. The resultant mobility values, in the respective TMDCs, are given by 94.03, 68.87, and 96.03 $cm^2/(V\ s)$. These obtained results are much smaller than those predicted by another theory [31] but are significantly compatible with experimental observations. For example, a range of saturated values of mobilities from 120 to 140 $cm^2/(V\ s)$ was experimentally measured in WS_2 in the range of temperature from 4 to 83 K [12].

In Fig. 9 we show the dependence of the peak value of K on the temperature. While $K^{\rm i}$ is expected to be nearly independent of T due to weak dependence of impurity scattering on T [66], the $K^{\rm ac}$ and $K^{\rm op}$ are expected to increase with the increase of temperature because the scattering rate due to phonons scattering increases [62]. Since the product $f_\alpha(1-f_{\alpha'})$ is very weakly dependent on T, the temperature variation of the $K^{\rm ac}$ and $K^{\rm op}$ is mainly through the factor $N_{\rm q}^v$, which increases with T. In the case of acoustic phonon scattering, $K^{\rm ac} \sim T\,\Gamma^{\rm ac}/[(X_\ell^{\rm ac})^2 + (\Gamma^{\rm ac})^2] \sim T^{1/2}$, which explains the $\sqrt{T}$-dependent $K^{\rm ac}$ as shown in Fig. 9. Meanwhile, in the case of the optical phonon scattering, $K^{\rm op} \sim (N_{\rm q}^{\rm op})^{1/2}$, which showed that $K^{\rm op}$ increases with the increase of temperature. Moreover, the value of the $K^{\rm i}$ is always bigger than that of $K^{\rm ac}$ and $K^{\rm op}$ in all four materials, with noting the factor of 10^4 in the case of impurity scattering.

The temperature dependence of the FWHM is shown in Fig. 10. Since the dependence of impurity scattering on T is very weak [66], we only show here the dependence of the FWHM on the temperature in the phonon scattering mechanism. Similar to the case of MOAC, the FWHM due to phonon scattering is found to increase with the increase of temperature. The $\sqrt{T}$-dependent FWHM in the case of acoustic phonon scattering is generated from the Lorentzian width, which is proportional to square root of T, while in the case

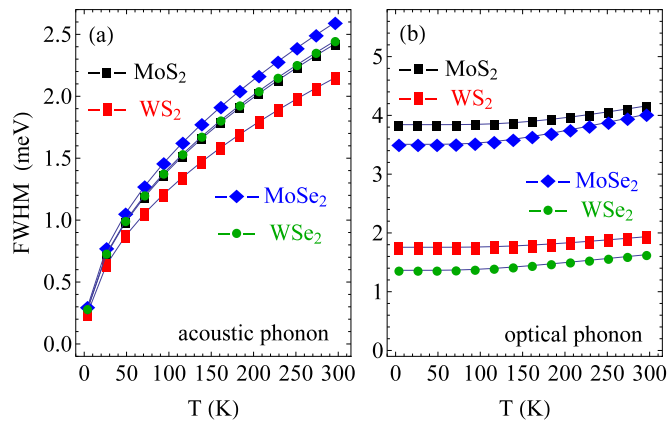

FIG. 10. Temperature dependence of the FWHM due to phonon scattering in different materials. The results are evaluated for one-photon process at $e\Delta_z = 37.75$ meV$/d$, $M_z, M_v \neq 0$, and $B = 10$ T.

TABLE IV. SO-phonon modes in substrates used in the numerical calculation. The characteristics of HfO_2 and SiO_2 are taken from Ref. [67], of ZrO_2 are from Ref. [70], and of h-BN are from Ref. [35].

	HfO_2	ZrO_2	SiO_2	h-BN
κ_0	22.00	24.0	3.90	5.09
κ_∞	5.03	4.00	2.40	4.10
$\hbar\omega_{SO}^{(1)}$ (meV)	21.60	25.02	58.90	101.70
$\hbar\omega_{SO}^{(2)}$ (meV)	54.20	70.80	156.40	195.70

of the optical phonon the T dependence of FWHM results from the proportion to the factor $(N_q^{op})^{1/2}$ of the Lorentzian width. Moreover, in the region of the low temperature, the effect of the temperature on the FWHM is negligible in the case of the optical phonon but is significant in the case of the acoustic phonon. This reveals that the acoustic phonon still plays an important role in the low-temperature regime. Besides, similar to the results shown in Fig. 8, for the acoustic phonon scattering the $MoSe_2$ depicts the strongest FWHM, while the MoS_2 shows the strongest one in the case of optical phonon.

C. Surface optical phonon scattering

For monolayer TMDCs on different substrates, just like graphene [29], the surface optical (SO) phonons interact with the carriers by an effective electric field [66,67]. In this case, the carrier-SO phonon coupling matrix element is given as [68,69]

$$\left|g_{\mathbf{q}}^{SO}\right|^2 = \frac{e^2\hbar\omega_{SO}^{(\lambda)}}{2S_0\varepsilon_0 q}\kappa^* e^{-2qd_i}, \tag{37}$$

where $\hbar\omega_{SO}^{(\lambda)}$ is the SO-phonon energy with $\lambda = 1, 2$ being the mode index. Furthermore, $\kappa^* = (\kappa_\infty + 1)^{-1} - (\kappa_0 + 1)^{-1}$ with κ_∞ and κ_0 being the static and optical dielectric constant of substrates, and d_i is the equilibrium distance between the TDMCs sheets and substrates. The material parameters of the substrate used in numerical calculation are listed in Table IV. Using the matrix element given in Eq. (37), the expression for MOAC is found as follows:

$$K^{SO}(\Omega) = \frac{e^2\hbar\omega_{SO}^{(\lambda)}\sqrt{2}}{2V_0\varepsilon_0\alpha_c^3}\kappa^* \sum_{\alpha,\alpha'\alpha''} G(\alpha)\Big\{\mathcal{P}^{(1)}_{\alpha',\alpha''}\big[N^{SO,-}_{\mathbf{q},\lambda} \times \delta\big(X^{SO,-}_{1,\lambda}\big) + N^{SO,+}_{\mathbf{q},\lambda}\delta\big(X^{SO,-}_{1,\lambda}\big)\big] + \frac{\alpha_0^2}{8\alpha_c^2}\mathcal{P}^{(2)}_{\alpha',\alpha''} \times \big[N^{SO,-}_{\mathbf{q},\lambda}\delta\big(X^{SO,-}_{21,\lambda}\big) + N^{SO,+}_{\mathbf{q},\lambda}\delta\big(X^{SO,-}_{2,\lambda}\big)\big]\Big\}, \tag{38}$$

where $N^{SO}_{\mathbf{q},\lambda}$ is the distribution function of SO phonon of energy $\hbar\omega_{SO}^{(\lambda)}$, the arguments of delta functions $X^{SO,\pm}_{\ell,\lambda}$ are given in the same form as $X_\ell^{op,\pm}$ [see Eq. (34)] but with $\hbar\omega_{op}$ replaced by $\hbar\omega_{SO}^{(\lambda)}$. Furthermore, $\mathcal{P}^{(k)}_{\alpha',\alpha''}$ is the dimensionless quantity defined as follows:

$$\mathcal{P}^{(k)}_{\alpha',\alpha''} = \int_0^\infty x^{k-1/2} e^{-2d_i\sqrt{2x}/\alpha_c} |J_{\alpha',\alpha''}(x)|^2 dx. \tag{39}$$

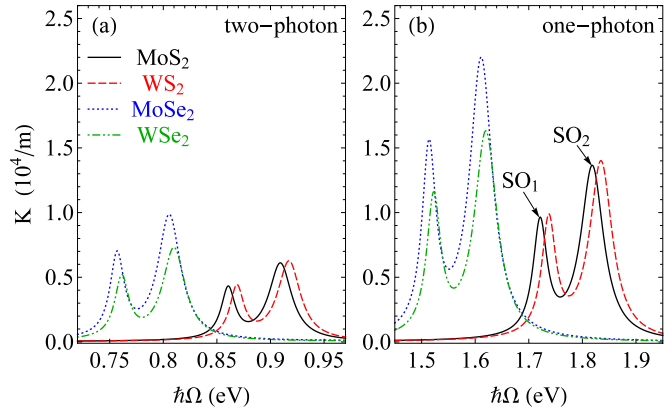

FIG. 11. The MOAC due to carrier-SO-phonon in monolayer TMDCs on SiO_2 substrate as a function of photon energy at $e\Delta_z = 37.75$ meV$/d$, $M_z, M_v \neq 0$, $B = 10$ T, $T = 4$ K, and $d_i = 0.4$ nm. (a) and (b) Two- and one-photon processes, respectively.

The Lorentzian width for the case of SO-phonon scattering is

$$\left(\Gamma^{\pm,SO,\lambda}_{\alpha,\alpha'}\right)^2 = \frac{e^2\hbar\omega_{SO}^{(\lambda)}}{8\pi\sqrt{2}\alpha_c}\kappa^*\mathcal{P}^{(0)}_{\alpha',\alpha''}N^{SO,\pm}_{\mathbf{q},\lambda}\delta_{s,s'}. \tag{40}$$

Here the expression for $\mathcal{P}^{(0)}_{\alpha',\alpha''}$ is treated from Eq. (39) for $k = 0$.

We now study the contribution of the two separate SO-phonon modes to the MOAC. In Fig. 11 we show the MOAC due to SO-phonon interaction in monolayer TMDCs/SiO_2 system as a function of photon energy. The SO-phonon scattering was indicated to have a vital role in the transport properties of the TMDCs/substrate system, especially when the distance between the monolayer TMDCs and the substrate is small [66]. Indeed, at the distance of $d_i = 0.4$ nm, for example, the MOAC intensity due to the SO-phonon scattering obtained here is about 100 times higher than those caused by both intrinsic acoustic and optical phonon scatterings [see Figs. 7(a) and 7(b)]. However, these values are still much smaller than those in the case of impurity scattering [see Fig. 4(a)]. In comparison between the two SO-phonon modes, with its higher energy, SO_2-phonon mode depicts not only a bigger contribution to the MOAC intensity but also the larger values of the absorbed photon energies in both one- and two-photon processes. This result fits well with those evaluated for graphene [49] as well as for monolayer MoS_2 [27] on different substrates. Moreover, since the energies of SO_1 mode and intrinsic optical phonons are almost the same, the peak positions due to SO_1-phonon mode and the intrinsic optical phonon are almost the same, while the peak position due to SO_2-phonon mode is located in a much higher energy range.

To understand the combined effect of different substrates and magnetic field on the transport properties, in Fig. 12 we show the MOAC in WS_2/substrate systems as a function of photon energy for different magnetic fields. The effect of the magnetic field on the MOAC is mainly led by the term $\alpha_c^{-3} \sim B^{3/2}$ [see Eq. (38)] resulting in the increasing of MOAC intensity and the blueshift with the magnetic field. This result fits well with those reported for the conductivity in graphene [35] and the magneto-optical transitions in MoS_2 on different

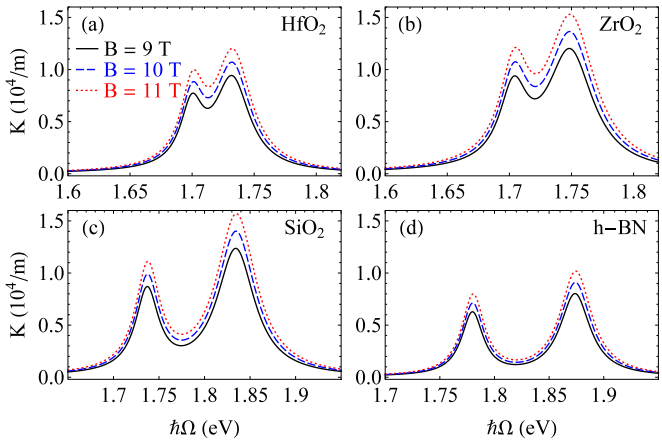

FIG. 12. The MOAC due to carrier-SO-phonon in monolayer WS_2 on different substrates versus photon energy for different magnetic fields. The results are evaluated for one-photon process, at $e\Delta_z = 37.75$ meV$/d$, $M_z, M_v \neq 0$, $T = 4$ K, and $d_i = 0.4$ nm.

substrates [36]. Meanwhile, the effect of different substrates on the MOAC intensity is mainly decided by their coupling matrix element with the carriers, which is expressed through the reduced quantity $\hbar\omega_{\rm SO}^{(\lambda)}\kappa^*$. Since SiO_2 has the biggest value of the carrier-SO-phonon scattering, the MOAC intensity in this substrate is the strongest, followed by that of ZrO_2, while h-BN exhibits the smallest one. Besides MOAC intensity, the substrates also affect another characteristic of MOAC, its position for example, through their finite and pretty large SO-phonon energies. In both case of SO_1 and SO_2-phonon interaction, with the smallest SO-phonon energies, the peak positions in HfO_2 substrate show the smallest shift, followed by that of ZrO_2, and then of SiO_2, while the peak positions in h-BN display the largest shift. In other words, the peak position shift under the effect of the substrates is followed by the order of $HfO_2 < ZrO_2 < SiO_2 <$ h-BN.

Finally, the influence of different substrates on the FWHM is presented in Fig. 13, where the FWHM of the absorption peaks due to SO-phonon interaction is plotted as a function of B for different substrates. Since the major purpose of this part is to study the influence of the substrates on the FWHM,

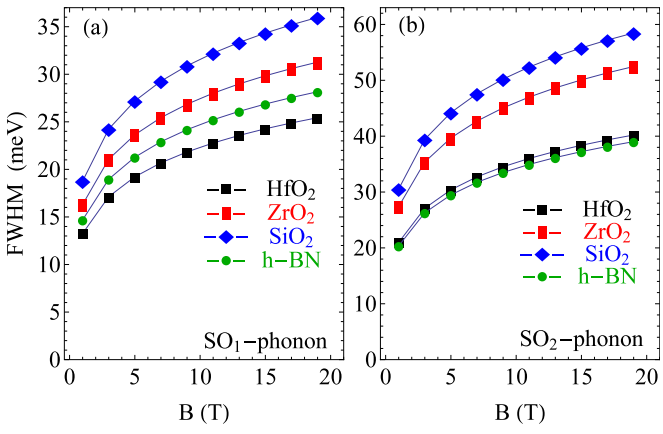

FIG. 13. The FWHM of the peaks shown in Fig. 12 versus the magnetic field. (a) and (b) SO_1 and SO_2 phonons, respectively.

we only present here for the monolayer WS_2, for example, but the results can be also validated for other TMDCs. The mainstream of the increase of FWHM with the magnetic field is also observed in the case of SO-phonon scattering, just like in other types of interactions: Impurity as well as intrinsic acoustic and optical phonon, but with a different rate. While the FWHM increases with the same $B^{1/2}$ rule in the cases of impurity and intrinsic phonons scattering, for the SO-phonon interaction, the FWHM increases with the $B^{1/4}$ rule, which is guided by the fact that the Lorentzian width in the case of SO-phonon interaction is proportional to $\alpha_c^{-1/2} \sim B^{1/4}$ [see Eq. (40)]. This means that in the case of SO-phonon interaction, the increase rate of the FWHM is smaller than that of the impurity and the intrinsic phonons interactions. Moreover, because of the strong SO-phonon couplings, the value of FWHM induced by this type of interaction is much bigger than those caused by the intrinsic phonons scattering. Besides, the result shown in Fig. 13 also reveals that the effect of two individual SO-phonon modes on the FWHM is similar, except that the FWHM due to SO_2-phonon interaction is bigger because of its bigger energy in comparison with that of SO_1 phonon. Similar to the case of MOAC, the effect of different substrates on the FWHM is also mainly guided by their carrier-SO-phonon coupling matrix element. With the strongest carrier-phonon coupling, the FWHMs in SiO_2 substrate have the highest values in both cases of SO_1 and SO_2 phonons, followed by that of ZrO_2. Whereas for the lowest value of the FWHM, there is a difference between the two individual SO-phonon modes. For the SO_1-phonon mode, the HfO_2 substrate shows the smallest FWHM caused by its smallest value of $\hbar\omega_{\rm SO}^{(1)}\kappa^*$ while the h-BN one exhibits the smallest FWHM in the case of SO_2-phonon scattering.

IV. SUMMARY AND CONCLUSIONS

We have studied the magnetotransport properties of monolayer TMDCs including different types of carrier scatterings. At the zero-magnetic field, in each material, the spin splitting in the conduction (valence) band is equal to $|\lambda_c|$ (λ_v) due to the combined action of the spin and valley splittings. The combined influence of the strong SOC and the Zeeman fields has doubled LLs but has not changed the energy gap of monolayer TMDCs. Nevertheless, this combined effect does not allow any new inter-LL transitions. The effect of the electric field depends on its direction. With a suitable choice of direction, the electric field can be used as a fruitful tool to open the band-gap energy of monolayer TMDCs. Because of the strong SOC effect in the monolayer TMDCs, the absorption spectrum is separated into two individual peaks corresponding to spin-up and spin-down cases, which are located in the visible region (one-photon absorption process), caused by their large band gap. Among these peaks, with stronger spin splitting effect, the peaks generated from the spin-down case are always located on the right-hand side of the spin-up ones in both one- and two-photon cases.

Among three types of scattering, the MOAC intensity in the case of impurity interaction is the strongest for the present choice of $n_i = 10^{13}$ m^{-2}, followed by that of the SO phonon, and the intrinsic phonons one is the weakest. Meanwhile, the FWHM induced by the SO-phonon scattering are biggest due

to their big SO-phonon energies, the values of the FWHM in the other two scattering types are almost the same. In comparison among the four materials, the MOAC intensity in $MoSe_2$ is always the biggest in three scattering types. Meanwhile, with the largest band gap, the peak position in WS_2 is always located in the highest value of the energy region. Since the nature of different scattering mechanisms is different, the order of the FWHM value due to different materials in different types of scattering is not uniform. With the smallest value of ε_r, WS_2 shows the highest value of the FWHM via impurity scattering, while $MoSe_2$ and MoS_2 display the biggest via intrinsic acoustic and optical phonons scattering, respectively. Besides, among four different substrates, SiO_2 always shows its superiority. The evidence is that both MOAC intensity and FWHM value in the TMDCs/SiO_2 system are always the biggest. Finally, all of the materials offer competitive transport performances of carriers. With their large band-gap energy, monolayer TMDCs could be promising alternatives to the traditional semiconductors as well as the graphene in the nanodevices applications, especially in the visible range.

ACKNOWLEDGMENTS

This research is funded by the Vietnam National Foundation for Science and Technology Development (NAFOSTED) under Grant No. 103.01-2019.11.

APPENDIX A: THE FORM FACTOR

In this Appendix we will present the expression of the form factor shown in Eq. (17) in more detail. Inserting the eigenfunctions (8) and (9) into Eq. (17), and then using the formula shown in Eq. (7.377) of Ref. [71], we obtain the following expression, assuming $n < n'$:

$$J_{\alpha',\alpha}(q) = \sqrt{\frac{n!}{n'}} e^{iq_x x_0} e^{-u/2} (i\sqrt{u})^{n'-n} \Big[B^{\tau',p'}_{n',s'} B^{\tau,p}_{n,s} L^{n'-n}_{n}(u) + |\tau|^2 A^{\tau',p'}_{n',s'} A^{\tau,p}_{n,s} \sqrt{\frac{n'}{n}} L^{n'-n}_{n-1}(u) \Big], \tag{A1}$$

with $u = q^2\alpha_c^2/2$. Squaring the two sides of the above equation, and noting that $|\tau|^2 = 1$, we will obtain the expression for $|J_{\alpha',\alpha''}(q)|^2$ as shown in Eq. (17), where the state $|\alpha\rangle$ would be changed to $|\alpha''\rangle$. In the case of $\alpha = \alpha'$, the result will be reduced to

$$|J_{nn}(u)|^2 = e^{-u}\Big[\big|B^{\tau,p}_{n,s}\big|^2 L_n(u) + \big|A^{\tau,p}_{n,s}\big|^2 L_{n-1}(u) \Big]^2, \tag{A2}$$

which is similar to the one reported in Ref. [7].

APPENDIX B: DIMENSIONLESS INTEGRALS

Using equations from (A1) to (A4) of Ref. [51] the dimensionless integrals in Eq. (29) are explicitly expressed as follows for the one- and two-photon processes:

$$\mathcal{Q}^{(1)}_{\alpha',\alpha''} = \big(B^{\tau,p'}_{n',s'} B^{\tau,p''}_{n'',s''}\big)^2 (2k + j + 1) - 2\big(A^{\tau,p'}_{n',s'} A^{\tau,p''}_{n'',s''} B^{\tau,p'}_{n',s'} B^{\tau,p''}_{n'',s''}\big)\sqrt{k(k+j)} + \big(A^{\tau,p'}_{n',s'} A^{\tau,p''}_{n'',s''}\big)^2 (2k + j - 1), \tag{B1}$$

$$\mathcal{Q}^{(2)}_{\alpha',\alpha''} = \big(B^{\tau,p'}_{n',s'} B^{\tau,p''}_{n'',s''}\big)^2 \{2 + 6k(k+1) + j[j + 3(2k+1)]\} - 2\big(A^{\tau,p'}_{n',s'} A^{\tau,p''}_{n'',s''} B^{\tau,p'}_{n',s'} B^{\tau,p''}_{n'',s''}\big) \times (2k + j)\sqrt{k(k+j)} + \big(A^{\tau,p'}_{n',s'} A^{\tau,p''}_{n'',s''}\big)^2 \times \{2 + 6k(k-1) + j[j + 3(2k-1)]\}, \tag{B2}$$

which are valid for all possible intravalley transitions.

[1] H. Ochoa and R. Roldán, Phys. Rev. B **87**, 245421 (2013).
[2] K. S. Novoselov, A. K. Geim, S. V. Morozov, D. Jiang, M. I. Katsnelson, I. V. Grigorieva, S. V. Dubonos, and A. A. Firsov, Nature (London) **438**, 197 (2005).
[3] A. Zunger, A. Katzir, and A. Halperin, Phys. Rev. B **13**, 5560 (1976).
[4] Q. H. Wang, K. Kalantar-Zadeh, A. Kis, J. N. Coleman, and M. S. Strano, Nat. Nanotechnol. **7**, 699 (2012).
[5] G. Eda and S. A. Maier, ACS Nano **7**, 5660 (2013).
[6] C. M. Wang and X. L. Lei, Phys. Rev. B **92**, 125303 (2015).
[7] M. Tahir, P. Vasilopoulos, and F. M. Peeters, Phys. Rev. B **93**, 035406 (2016).
[8] M. Tahir and P. Vasilopoulos, Phys. Rev. B **94**, 045415 (2016).
[9] A. J. Chaves, R. M. Ribeiro, T. Frederico, and N. M. R. Peres, 2D Mater. **4**, 025086 (2017).
[10] G. Catarina, J. Have, J. Fernández-Rossier, and N. M. R. Peres, Phys. Rev. B **99**, 125405 (2019).
[11] B. Radisavljevic and A. Kis, Nat. Mater. **12**, 815 (2013).
[12] D. Ovchinnikov, A. Allain, Y.-S. Huang, D. Dumcenco, and A. Kis, ACS Nano **8**, 8174 (2014).
[13] A. A. Mitioglu, P. Plochocka, Á. Granados del Aguila, P. C. M. Christianen, G. Deligeorgis, S. Anghel, L. Kulyuk, and D. K. Maude, Nano Lett. **15**, 4387 (2015).
[14] R. Schmidt, A. Arora, G. Plechinger, P. Nagler, A. Granados del Águila, M. V. Ballottin, P. C. M. Christianen, S. Michaelis de Vasconcellos, C. Schüller, T. Korn, and R. Bratschitsch, Phys. Rev. Lett. **117**, 077402 (2016).
[15] Z. Wang, J. Shan, and K. F. Mak, Nat. Nanotechnol. **12**, 144 (2017).
[16] T. Smoleński, O. Cotlet, A. Popert, P. Back, Y. Shimazaki, P. Knüppel, N. Dietler, T. Taniguchi, K. Watanabe, M. Kroner, and A. Imamoglu, Phys. Rev. Lett. **123**, 097403 (2019).
[17] M. Koperski, M. R. Molas, A. Arora, K. Nogajewski, M. Bartos, J. Wyzula, D. Vaclavkova, P. Kossacki, and M. Potemski, 2D Mater. **6**, 015001 (2019).
[18] C. Chakraborty, K. M. Goodfellow, and A. Nick Vamivakas, Opt. Mater. Express **6**, 2081 (2016).
[19] A. Srivastava, M. Sidler, A. V. Allain, D. S. Lembke, A. Kis, and A. Imamoglu, Nat. Phys. **11**, 141 (2015).
[20] G. Aivazian, Z. Gong, A. M. Jones, R.-L. Chu, J. Yan, D. G. Mandrus, C. Zhang, D. Cobden, W. Yao, and X. Xu, Nat. Phys. **11**, 148 (2015).
[21] K. D. Pham, L. V. Tung, D. V. Thuan, C. V. Nguyen, N. N. Hieu, and H. V. Phuc, J. Appl. Phys. **126**, 124301 (2019).
[22] V. P. Gusynin, S. G. Sharapov, and J. P. Carbotte, Phys. Rev. Lett. **98**, 157402 (2007).

[23] M. Koshino and T. Ando, Phys. Rev. B **77**, 115313 (2008).
[24] B. D. Hoi, L. T. T. Phuong, and T. C. Phong, J. Appl. Phys. **123**, 094303 (2018).
[25] H. Yuan, M. S. Bahramy, K. Morimoto, S. Wu, K. Nomura, B.-J. Yang, H. Shimotani, R. Suzuki, M. Toh, C. Kloc, X. Xu, R. Arita, N. Nagaosa, and Y. Iwasa, Nat. Phys. **9**, 563 (2013).
[26] K. Shakouri, P. Vasilopoulos, V. Vargiamidis, and F. M. Peeters, Phys. Rev. B **90**, 125444 (2014).
[27] C. V. Nguyen, N. N. Hieu, N. A. Poklonski, V. V. Ilyasov, L. Dinh, T. C. Phong, L. V. Tung, and H. V. Phuc, Phys. Rev. B **96**, 125411 (2017).
[28] V. A. Margulis, J. Exp. Theor. Phys. **99**, 633 (2004).
[29] C. M. Wang and X. L. Lei, Phys. Rev. B **87**, 235403 (2013).
[30] Z. Li and J. P. Carbotte, Physica B **421**, 97 (2013).
[31] K. Kaasbjerg, K. S. Thygesen, and A.-P. Jauho, Phys. Rev. B **87**, 235312 (2013).
[32] K. Kaasbjerg, K. S. Bhargavi, and S. S. Kubakaddi, Phys. Rev. B **90**, 165436 (2014).
[33] K. S. Bhargavi, S. Patil, and S. S. Kubakaddi, J. Appl. Phys. **118**, 044308 (2015).
[34] I.-T. Lin and J.-M. Liu, Appl. Phys. Lett. **103**, 081606 (2013).
[35] B. Scharf, V. Perebeinos, J. Fabian, and I. Žutić, Phys. Rev. B **88**, 125429 (2013).
[36] Z.-W. Wang, R.-Z. Li, Y. Xiao, and Z.-Q. Li, Phys. Lett. A **380**, 3843 (2016).
[37] Z. Li and J. P. Carbotte, Phys. Rev. B **88**, 045417 (2013).
[38] Y. Ding, Y. Wang, J. Ni, L. Shi, S. Shi, and W. Tang, Physica B **406**, 2254 (2011).
[39] Z. Jin, X. Li, J. T. Mullen, and K. W. Kim, Phys. Rev. B **90**, 045422 (2014).
[40] D. Xiao, G.-B. Liu, W. Feng, X. Xu, and W. Yao, Phys. Rev. Lett. **108**, 196802 (2012).
[41] G.-B. Liu, W.-Y. Shan, Y. Yao, W. Yao, and D. Xiao, Phys. Rev. B **88**, 085433 (2013).
[42] A. Kormányos, V. Zólyomi, N. D. Drummond, and G. Burkard, Phys. Rev. X **4**, 011034 (2014).
[43] C. J. Tabert and E. J. Nicol, Phys. Rev. Lett. **110**, 197402 (2013).
[44] N. D. Drummond, V. Zólyomi, and V. I. Fal'ko, Phys. Rev. B **85**, 075423 (2012).
[45] D. Xu, H. He, R. Pandey, and S. P. Karna, J. Phys.: Condens. Matter **25**, 345302 (2013).
[46] N. D. Hien, N. Q. Cuong, L. M. Bui, P. C. Dinh, C. V. Nguyen, H. V. Phuc, N. V. Hieu, H. R. Jappor, L. T. T. Phuong, B. D. Hoi, L. C. Nhan, and N. N. Hieu, Physica E **111**, 201 (2019).
[47] W. Xu, R. A. Lewis, P. M. Koenraad, and C. J. G. M. Langerak, J. Phys.: Condens. Matter **16**, 89 (2004).
[48] W. Xu, Phys. Rev. B **57**, 12939 (1998).
[49] H. V. Phuc and L. Dinh, Mater. Chem. Phys. **163**, 116 (2015).
[50] S. L. Chuang, *Physics of Optoelectronic Devices* (Wiley, New York, 1995).
[51] H. V. Phuc and N. N. Hieu, Opt. Commun. **344**, 12 (2015).
[52] D. Dunn and A. Suzuki, Phys. Rev. B **29**, 942 (1984).
[53] T. Stauber, N. M. R. Peres, and F. Guinea, Phys. Rev. B **76**, 205423 (2007).
[54] M. P. Chaubey and C. M. Van Vliet, Phys. Rev. B **33**, 5617 (1986).
[55] H.-L. Liu, C.-C. Shen, S.-H. Su, C.-L. Hsu, M.-Y. Li, and L.-J. Li, Appl. Phys. Lett. **105**, 201905 (2014).
[56] A. Laturia, M. L. Van de Put, and W. G. Vandenberghe, NPJ 2D Mater. Appl. **2**, 6 (2018).
[57] Y. Wu, J. J. He, T. Han, S. Xu, Z. Wu, J. Lin, T. Zhang, Y. He, and N. Wang, Phys. Rev. B **99**, 121406(R) (2019).
[58] W.-K. Tse and A. H. MacDonald, Phys. Rev. B **84**, 205327 (2011).
[59] Z. Li and J. P. Carbotte, Phys. Rev. B **88**, 045414 (2013).
[60] N. Shon and T. Ando, J. Phys. Soc. Jpn. **67**, 2421 (1998).
[61] Z. Jiang, E. A. Henriksen, L. C. Tung, Y.-J. Wang, M. E. Schwartz, M. Y. Han, P. Kim, and H. L. Stormer, Phys. Rev. Lett. **98**, 197403 (2007).
[62] K. Kaasbjerg, K. S. Thygesen, and K. W. Jacobsen, Phys. Rev. B **85**, 115317 (2012).
[63] A. Thilagam, J. Appl. Phys. **119**, 164306 (2016).
[64] X. Li, J. T. Mullen, Z. Jin, K. M. Borysenko, M. Buongiorno Nardelli, and K. W. Kim, Phys. Rev. B **87**, 115418 (2013).
[65] E. J. Johnson and D. H. Dickey, Phys. Rev. B **1**, 2676 (1970).
[66] N. Ma and D. Jena, Phys. Rev. X **4**, 011043 (2014).
[67] B. Scharf, V. Perebeinos, J. Fabian, and P. Avouris, Phys. Rev. B **87**, 035414 (2013).
[68] N. Mori and T. Ando, Phys. Rev. B **40**, 6175 (1989).
[69] S. Fratini and F. Guinea, Phys. Rev. B **77**, 195415 (2008).
[70] A. Konar, T. Fang, and D. Jena, Phys. Rev. B **82**, 115452 (2010).
[71] A. Jeffrey and D. Zwillinger, *Table of Integrals, Series, and Products* (Elsevier, Amsterdam, 2007).